Photodiagnosis and Photodynamic Therapy 33 (2021) 102195

Contents lists available at ScienceDirect

Photodiagnosis and Photodynamic Therapy

journal homepage: www.elsevier.com/locate/pdpdt

Hyperspectral imaging assessment for radiotherapy induced skin-erythema: Pilot study

Ramy Abdlaty [a,b,*], Lilian Doerwald-Munoz [c], Thomas J. Farrell [c,d], Joseph E. Hayward [c,d], Qiyin Fang [b,e]

[a] Department of Biomedical Engineering, Military Technical College, Cairo, Egypt
[b] School of Biomedical Engineering, McMaster University, Ontario, Canada
[c] Juravinski Cancer Centre, Hamilton Health Sciences, Ontario, Canada
[d] School of Interdisciplinary Science, McMaster University, Ontario, Canada
[e] Department of Engineering Physics, McMaster University, Ontario, Canada

ARTICLE INFO

Keywords:
Skin cancer
Radiation therapy
Hyperspectral imaging
Skin erythema
Radiation toxicity

ABSTRACT

Skin cancer (SC) is a widely spread disease in the USA, Canada, and Australia. Skin cancer patients may be treated by many different techniques including radiation therapy. However, radiation therapy has side effects, which may range from skin erythema to skin necrosis. As erythema is the early evidence of exposure to radiation, monitoring erythema is important to prevent more severe reactions. Visual assessment (VA) is the gold standard for evaluating erythema. Nevertheless, VA is not ideal, since it depends on the observer's experience and skills. Digital photography and hyperspectral imaging (HSI) are optical techniques that provide an opportunity for objective assessment of erythema. Erythema indices were computed from the spectral data using Dawson's technique. The Dawson relative erythema index proved to be highly correlated (97.1 %) with clinical visual assessment scores. In addition, on the 7th session of radiation therapy, the relative erythema index differentiates with 99 % significance between irradiated and non-radiated skin regions. In this study, HSI is compared to digital photography for skin erythema statistical classification.

1. Introduction

Skin cancer (SC) is classified into non-melanoma skin cancer (NMSC) and melanoma skin cancer (MSC). MSC is life-threatening, but fortunately, it accounts for only 2 % of SC patients [1]. NMSC can be treated through several approaches [2], most commonly, surgery or local radiotherapy [3]. Elderly SC patients are frequently excluded from the surgical approach due to age-related comorbidities [3,4]. Radiotherapy treatment uses ionizing radiation (X-rays photons/electrons) [2] to produce a series of fatal DNA disruptions to control malignant tumor growth. Frequently, the prescribed dose of radiation is divided into a number of smaller doses, called "fractions" [5,6]. These fractions have upper and lower limits for daily dose (Gy/day) designed to achieve maximum therapeutic benefit and minimum tissue toxicity.

The toxicity of healthy skin is an undesirable side effect of radiation therapy. Some studies [7–10] have articulated that at least 85–95 % of radiotherapy-treated patients encountered adverse side effects [59]. These side effects vary in intensity from mild (erythema) to severe (skin necrosis) and depend on several human-related parameters [7,8,10–12]. The parameters which are highly correlated with the adverse skin reactions were studied formerly [13–16]. Age, gender, radiation type, and the treated body part of the patient were found to be the most dominating parameters, while the dose level was less dominant [17–19]. The surveys done on irradiated patients stated that radiation induced skin toxicities vary in its nature, time to become visible and severity [7,20]:

1 The earliest skin response manifests as transient skin redness (skin erythema) which becomes apparent in under or it can linger visibly undetected up to 15 fractions.
2 The soreness of the skin that takes place due to the fluctuating death in the amount of epidermal basal cells. It typically occurs after 15 fractions. The consequence of skin soreness is either a dry or wet desquamation [9].
3 A long-term skin response (dermal ischemia and necrosis) may come about 2–4 months after irradiation.

* Corresponding author at: Department of Biomedical Engineering, Military Technical College, Cairo, Egypt.
E-mail address: ramy.elghwas@mtc.edu.eg (R. Abdlaty).

https://doi.org/10.1016/j.pdpdt.2021.102195
Received 4 August 2020; Received in revised form 6 January 2021; Accepted 20 January 2021
Available online 27 January 2021

4 Late skin damage, such as the development of telangiectasia and severe necrosis might ensue a year later.

Erythema was chosen as a suitable radiation-induced skin toxicity to study with optical techniques over the course of treatment. Erythema (skin redness) is an inflammatory response to injury caused by ionizing radiation. Erythema is the result of damage to the basal cells of the epidermis. Tissue injury causes vasodilation, which changes perfusion within the dermis layer. The light within the visible-NIR spectra penetrates the human skin with 2 mm depth [22] and thus, imaging in the VNIR region can probe the epidermal layer to capture the erythema.

Efforts were undertaken to apply several techniques in objectively evaluating radiation-induced erythema [18,20,22–25]. Despite the diversity of the former objective techniques [26–28], visual assessment is still considered the gold standard for skin erythema evaluation [29]. However, visual assessment is far from ideal, since it is subjective and strongly dependent on observer experience and human factors including visual acuity. Two assessment techniques, Diffuse reflectance spectroscopy (DRS) [30–32] and digital imaging [33–35] were studied as objective alternatives to VA. Yet, both were found unsatisfactory by clinicians. Clinicians criticize DRS because the region inspected is small and requires skin contact. Digital imaging is criticized because it provides limited spectral details and depends on the photographer's skills. Hence, a technique that overcomes these shortcomings may be better accepted by clinicians for clinical work.

Hyperspectral imaging (HSI) is a rapidly emerging optical technique that is the objective of many fields of research [36–39] including medicine [40]. HSI captures multiple frames of sequential spectral bands for a well-defined region. A radiance spectrum can be collected for each pixel recorded in the stack of frames. Thereby, HSI rises above the limitations of DRS and digital imaging and overcomes the subjectivity and experience-based disadvantages of the gold standard but is complex and time consuming.

This study is investigating the potential of HSI for objectively quantifying radiotherapy-induced erythema. This study will: (1) analyze the visual assessment scores, (2) compute the daily diffuse reflectance of the skin, (3) estimate the skin's chromophores concentration using least square fitting, and 4) apply a statistical classification upon HSI and corresponding digital color images for the skin erythema and compare the results.

2. Materials and methods

2.1. Clinical protocol

The entire clinical work was conducted with the approval of our research ethics board committee for human experiments. Written consent was given by all participating subjects along with a schedule of both study and treatment sessions. The patients were instructed not to apply any topical agent or skin dressing except under the recommendation of the oncologist.

Eight skin cancer patients were consented to participate in the study, however, the data for only five patients were included in this study. The data for the remaining three patients were not included on the basis of the study's exclusion criteria. The demographic data of the five patients is displayed in Table 1. The average age was 75 years old, with 2:3 female to male ratio, respectively. All the recruited patients were diagnosed with NMSC; either basal cell carcinoma (BCC) or squamous cell carcinoma (SCC) and received at least 10 radiation fractions during treatment. The treated location, for the recruited patients, varied between the arms, legs and face regions. The type of radiation prescribed was either electrons or x-rays.

The daily hyperspectral imaging and skin assessments were scheduled before each patients' treatment. At the session, a radiotherapist assessed the skin for erythema, assigned erythema grades and documented any relevant symptoms or features. A special reclining chair was used to seat the patients and reproduce their daily position for imaging. A platform was designed and built to house the imaging instrumentation and help maintain a constant relative patient-instrumentation placement. For each patient a treatment field, referred to as the region of interest (ROI) as marked on the patient skin with a marker to ensure reproducibility. A transparent film was used as a template to reproduce the ROI marks, which included permanent landmarks and features such as skin folds, moles or freckles. The template helped reposition the ROI in the event that the marks were removed or faded during the weekends. The template also had information such as orientation and image edges, which helped registering consequent images during analysis. An image of one patient's treatment ROI is shown in Fig. 1.

2.2. Visual assessment

On a daily basis, a study questionnaire was completed verbally by the patients. The intent of the questionnaire was to document the patients' activity from the previous day along with any skin reactions noted during the session. Topical agents applied by the patient in the ROI were also documented. The patients' answers and erythema scores were recorded on a paper-based tracking system and as a digital record. Skin erythema scores were graded on a 5-steps scale as shown in Table 2.

The scale was designed in consultation with the radiotherapists at

Fig. 1. Picture of a ROI is marked on the knee one of the participants. The marks were used as a reference for daily radiation treatments. To verify clinical procedure reproducibility, a transparent film template with the patient marks was created as a backup in case the original marks faded.

Table 1
Demographic data of the patients participating in the study.

Patient	Gender	Age	Histology	Radiation type	Energy	Bolus	Dose (cGy)	Fractions	Site
1	Female	88	SCC	Electrons	9 MeV	1.5 cm	5000	20	Left tibia
2	Female	56	BCC	X-rays	65 KVp	–	5000	20	Left forearm
3	Male	68	BCC	X-rays	65 KVp	–	4250	10	Left cheek
4	Male	85	BCC	Electrons	12 MeV	1cm	4250	10	Right ear
5	Male	75	SCC	X-rays	130 KVp	–	4250	10	Left temple

Table 2
Clinical assessment of skin erythema 5-steps grading scale.

Erythema level	Score (%)	Description
Normal	0	No visible erythema
Very faint	25	Skin has a very light pink color
Faint	50	Skin reaction is more apparent with clear borders but is still pink with more intensity.
Bright	75	Erythema is apparent in bright pink and borders are clearly defined.
Very Bright	100	Skin is bright red, borders are very well defined, capillaries and bruising may be visible.

Juravinski Cancer Center. Each erythema level was assigned as a percentage score. Frequently, the patient's skin developed more than one erythema level within the ROI but rather inhomogeneous distinct erythema levels.

2.3. Digital color imaging

A digital camera was used to capture daily images of the patients' ROI. The image was not limited to the marked ROI, The digital images also captured an area of normal skin outside the treatment field. The non-irradiated skin region within the captured frames enabled tracking of daily normal skin status. Digital imaging was repeated three times at each session to reduce human-based errors. The digital color images were captured by a high definition digital video camera (HYUNDAI-HDMI-768) which has a 16 Mega-pixels sensor along with a 3″ LCD display to adjust the FOV (field of view). The camera was equipped with an objective lens F/3.2, f = 7.5 mm. The camera dimensions were 110 × 58 × 50 mm and weighed 240 g. The illumination and the perspective view were considered to be the same along the entire study. Color images were used as a record of the skin appearance. In addition, it facilitated the cross-validation of the clinical erythema scores among different radiotherapists assessing the skin.

2.4. Hyperspectral imaging

A custom-made HSI system, developed and characterized elsewhere [41], was used to acquire the patients' data. For this purpose, the patient's FOV is illuminated with a halogen light source emitting in the VNIR spectra. The light was shone on the patients from different directions to reduce the shadow effect.

The patient's ROI back-reflected light is collected at the focal plane of a zoom lens. An optical relay is used to convey the captured FOV through the optical configuration using an achromatic lens pair. The collimated beam output of the primary relay lens is transmitted through a polarizing beam splitter (PBS), which permits the linearly vertical polarized light component to go through while reflecting the horizontally polarized component. The horizontally polarized component is folded toward a half-wave plate for a 90° degrees polarization rotation. By then, both PBS light components are directed onto an acousto-optic tunable filter (AOTF) [42]. Tweaking the horizontal component of the polarized input ray contributes to raising the system throughput since the involved AOTF cell is optimized for linearly vertical polarization. AOTF crystal derived from an RF synthesizer diffracts tunable light bandwidth angularly, separating it from the original beam. The second optical relay lens is aligned to receive only the separated diffracted light band and focus it on the detector.

The HSI imaging detector (Ximea MQ042rg-CM Enhanced-IR) incorporated in the system is a monochromatic CMOS sensor-based camera. It has an active sensor area of 11.24 mm^2 with 2048 × 2048 pixels and a pixel pitch of 5.5 μm. The camera exposure time extends from ~25 μsec up to 1 s and supports up to 90 frames per second. A skin region of approximately 11 × 11 cm^2 was considered to involve both irradiated and non-irradiated regions, resulting in a spatial resolution of 0.05 mm/ pixel.

A developed code by C-language was used to synchronize the AOTF and camera operation simultaneously through a user-friendly interface. The single hyperspectral data set involves three datacubes: the first for the patient ROI, the second is for a standard white diffuse reflectance surface (SRS-99-010, Labsphere, North Sutton, New Hampshire), and the third for the camera dark current. The white standard surface datacube is collected right after the imaging the patient, in order to maintain the same position and illumination conditions. The camera dark current data is collected while the zoom lens cap is on and all lights are off. Each datacube includes 89 narrowband images bounded by the spectral range of 450:850 nm. The integration time for capturing one band image is one second, and thus a single datacube takes 89 s. Spectral data sets, likewise digital color imaging, were repeated 3 times to minimize human errors. A simulation for the study's imaging session is shown on a volunteer in Fig. 2.

2.5. Data analysis

For each patient, the skin erythema clinical score was tabulated in his/ her file day-to-day. Besides the clinical score, the captured digital color images, and the spectral HSI datacubes, for the corresponding same day, were filed and labeled by the patient code and the date of data acquisition.

2.6. Visual assessment score

The erythema score (S) is computed as the summation of the visual erythema grade (G), assessed by the radiotherapist, multiplied by the corresponding occupied percentage area within the treatment field, as shown in Eq. (1). To give an example, a score of 1.0 is equivalent to a bright erythema present on the entire treatment field.

$$S = \sum_{i=1}^{4} G_i * A_i \quad (1)$$

2.7. Spectral reflectance computation

The patients' daily datacube is preprocessed for analysis in two consecutive steps. The first step is to subtract the dark datacube pixel intensity (I_{dark}) from both the patient's raw datacube (I_{ROI}) along with the reference white standard pixel intensity (I_{ws}). The dark datacube represents the existing background. The second step is to divide the patient data by the corresponding background-free white reference data. The former preparation steps are mathematically displayed in Eq. (2) and applied using Image-J software [43].

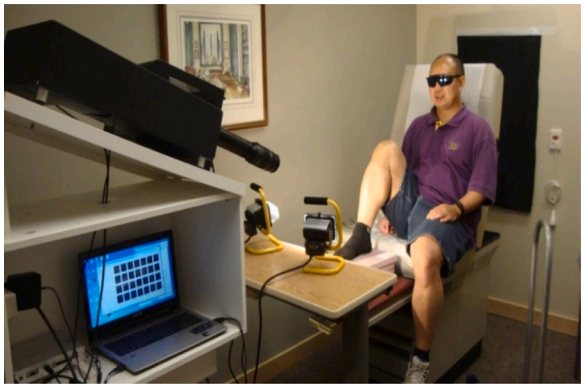

Fig. 2. A volunteer simulating patient is seated in order to be prepared for hyperspectral imaging. The treatment field is supposed to be on the right leg, therefore, it is illuminated from two sides to avoid the shadow effect. Sunglasses were worn to protect the subject eyes.

$$R_{ROI} = \frac{I_{ROI} - I_{dark}}{I_{ws} - I_{dark}} \quad (2)$$

The resultant output of Eq. (2) is the spectral-resolved diffuse reflectance datacube. Since each datacube is composed of 89 narrowband images, image registration is required for processing. For registration purposes, the narrowband image with the central wavelength $\lambda =$ 600 nm was assigned to be the reference band. The aforementioned narrowband image is assigned since it is located on the highest point of the spectral performance for our employed hyperspectral imaging system. The reference band is used for image registration to eliminate the patient's movements using Image-J software. A Sample of the datacube narrowband images at few wavelengths (560, 580, 650, 700, and 840 nm), along with a digital color image for the same patient ROI is displayed in Fig. 3. All the images, spectral and color, were taken at the same time point (13th session) of the radiotherapy treatment.

The skin erythema implies a large variation of the skin content of the hemoglobin chromophore. The hemoglobin is distinguished by two spectral absorption peaks at around wavelengths 560 and 580 nm. Therefore, the highly concentrated hemoglobin regions look darker in the spectral narrowband images centered at the aforementioned wavelengths [44,45]. The penetration depth at the green spectra, including the 560 and 580 nm bands, is limited to fractions of mm range [46], which restricts the visibility to superficial capillaries. However, deeper skin information could be achieved at longer wavelengths since the visible skin chromophores are less absorptive and thus, light can travel further down to a couple of millimeters. For instance, the longer wavelength bands show a pale shadow, due to erythema, in the region of increased hemoglobin content as seen at 650 nm, and 700 nm narrowband images. At the narrowband image of 840 nm central wavelength, all the chromophores display absorption minima.

The skin erythema visibility is not only because the red portion of the incident light was greatly scattered, but also due to the fact that green portion was intensely absorbed as shown in Fig. 4. As the melanin concentration of the epidermal layer is indeterminate, the estimated hemoglobin concentration is considered apparent in the case of a single-layered tissue model. In fact, the apparent hemoglobin concentration is an indicative value, but unlike the true concentration it is found in ex-vivo dermal skin tissue. However, it is still a quantitative index for erythema percentage variation if a hemoglobin baseline concentration is considered.

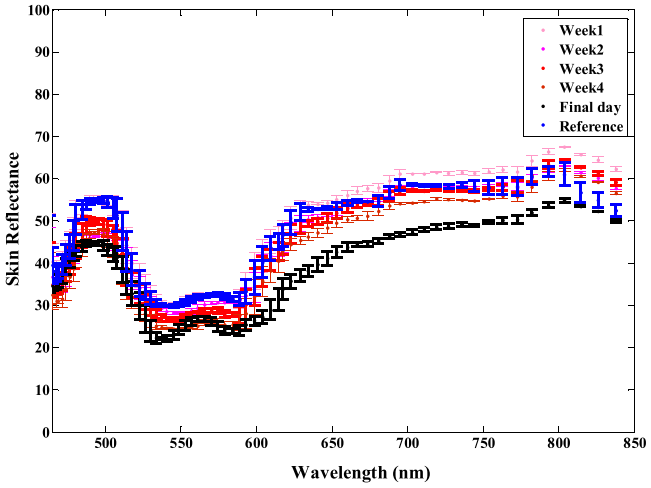

Fig. 4. Patient diffuse reflectance spectra for the treatment field of skin on treatment days (reddish dots), and at the end of treatment (black dots). A reference diffuse reflectance spectrum for non-irradiated skin region is plotted (blue dots). The amount (percent) of reflected light is temporally decreasing in the green region in a gradual style rather than the corresponding arbitrary behavior in the red one.

2.8. Erythema index computation

The erythema index, proposed by Dawson [47] and cited more than 460, is a common computational method, for probing skin chromophores change in concentration out of measured diffuse reflectance. The method is based on computing the area under the curve (AUC) of the logarithm of the skin diffuse reflectance reciprocal (LRR) in the visible region (510−610 nm). This spectral region is comprised of two of the hemoglobin distinguished absorption peaks. Dawson's erythema index (DEI) is computed according to Eq. (3):

$$\boldsymbol{DEI} = 100^{*}\left[\boldsymbol{r} + \frac{3}{2}(\boldsymbol{q} + \boldsymbol{s}) - 2(\boldsymbol{p} + \boldsymbol{t})\right] \quad (3)$$

Hereby, p, q, r, s, and t are symbols expressing the LRR values of the measured data at the five wavelengths 510, 540, 560, 580, and 610 nm,

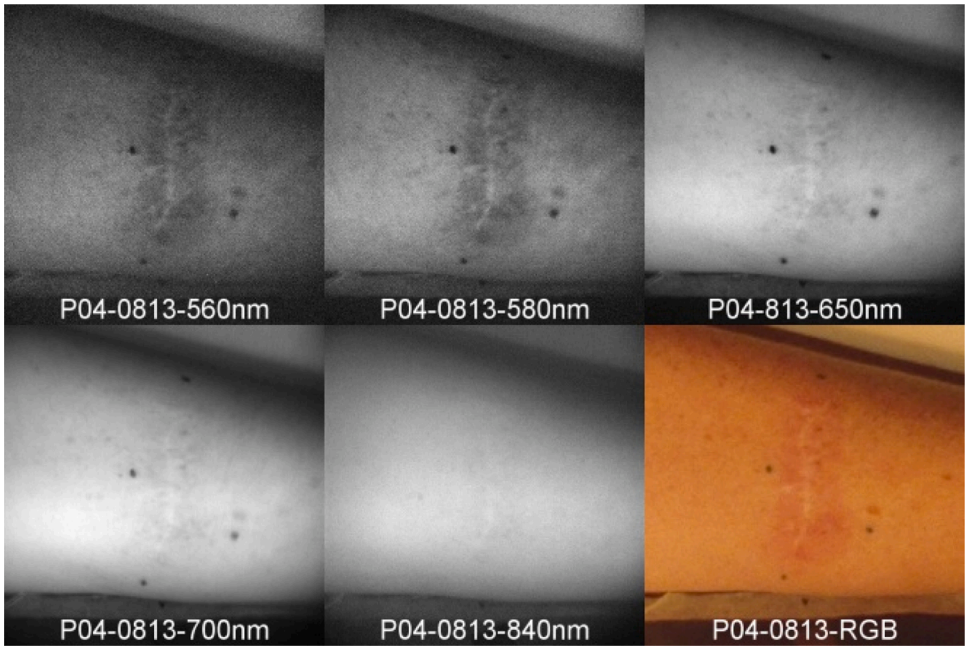

Fig. 3. Sample of the datacube band images at selected wavelengths (560, 580, 650, 700, and 840 nm), along with a digital color image for the same patient ROI. All the images, spectral and color, were taken at the same time point (13th session) of irradiation. The 560, 580 nm bands are highlighting the hemoglobin absorption, while the 650, 700 nm are representing the melanin correction bands, and the 840 nm NIR band is showing the low absorption of the majority of skin chromophores (hemoglobin, melanin, and water).

respectively. According to the HSI instrument specifications the former wavelengths were not exactly reachable, so we replaced the p, q, r, s, and t LRR exact values by the corresponding LRR average value for the adjacent spectral range $(\lambda_{p,q,r,s,t} \pm 5\ nm)$.

The melanin, chromophore is an influential component in the visible diffuse reflectance spectroscopy of skin. As a result, melanin's effect needs to be compensated in the erythema index computation by using skin reflectance data at two wavelengths (650&700 nm) to compute Dawson's melanin index (DMI) [48]. The aforementioned wavelengths were selected because melanin's spectral absorbance is proportional to its concentration at these two spectral points, as well as the low absorbance of the hemoglobin in this spectral region [47]. DMI is computed with the same averaging range $(\lambda \pm 5\ nm)$ for the wavelengths applied t Eq. (4).

$$DMI = 100^{*}[Log_{10}\left(\frac{1}{(\overline{R}_{645,650,655}}\right) - Log_{10}\left(\frac{1}{(\overline{R}_{695,700,705}}\right) + 0.015] \quad (4)$$

The corrected erythema index (DEI_c) is computed using DMI by applying the formula shown in Eq. (5), where $\gamma = 0.04$ is an empirically derived balancing constant to avoid negative values as a result of other existing but non-significant skin chromophores.

$$DEI_c = \left(100^{*}\left[r + \frac{3}{2}(q+s) - 2(p+t)\right]\right)^{*}(1 + (\gamma^{*}DMI)) \quad (5)$$

In this study, the participating patients were seen on a daily basis to monitor the development of erythema due to irradiation. For this reason, day-to-day erythema assessment might be needed for clinical purposes. Thus, relative Dawson erythema index (DEI_r) is calculated. DEI_r is computed by subtracting DEI_c for one day from the previous day. The erythema relative index provides a more informative figure for the skin color alteration since it avoids the effect of systemic errors.

2.9. Estimation of skin chromophores

Diffuse reflectance data acquired by spectroscopic based instrumentation need to be interpreted using a model to account for the propagation of the light inside biological tissues. In our study, the model can be approximated by a perpendicular light source illuminating a semi-infinite, homogeneous slab. Quantitatively estimating the concentrations of the main chromophores can be accomplished with a conditional least-square fitting of the skin-absorbers' extinction coefficients. The logarithmic reciprocal of the measured diffuse reflectance data $R(\lambda)$ is optimally fitted by the sum of the dominant skin chromophores' extinction coefficients $\varepsilon_n(\lambda)$ in the applicable spectral region, multiplied by their concentrations C_n as shown in Eq. (6) [49]:

$$log_{10}\left(\frac{1}{R(\lambda)}\right) = \sum_n C_n{}^{*}\varepsilon_n(\lambda) \quad (6)$$

Three chromophores are dominant in the visible spectrum (500−840 nm; the oxygenated fraction of hemoglobin (HbO2), the deoxygenated fraction of hemoglobin (Hb), and melanin. A minor effect might be attributed to other skin chromophores such as water and fats. This effect can be compensated by adding a constant (R_c) as in Eq. (7):

$$-log_{10}\,[R\,(\lambda)\,] = C_{oxy}.\,\varepsilon_{oxy}(\lambda) + C_{deoxy}.\,\varepsilon_{deoxy}(\lambda) + C_m.\,\varepsilon_m(\lambda) + R_c. \quad (7)$$

Where the terms: C_{oxy}, $\varepsilon_{oxy}(\lambda)$, C_{deoxy}, $\varepsilon_{deoxy}(\lambda)$, C_m, *and* $\varepsilon_m(\lambda)$ are the concentrations and extinction coefficients of HbO2, Hb, and melanin, respectively.

2.10. Image classification

Classification in the HSI context is the process of allocating distinct data classes within a hyperspectral datacube. For allocating the separate classes, a step-wise procedure is followed. The first step is data normalization to a reference (the white standard in our case). The second step is to reduce the noise in the collected data via a smoothing technique. Various approaches are available to reduce the background noise in an image including software enhancement or involving high-end optical filters. The latter approach is an expensive one. However, software enhancement using for example Wiener filter is considered an efficient noise reduction approach [50]. Wiener filter statistically estimates the meaningful information out of the original noisy data with a lossless amount of real information. It uses the minimum mean square error method to exclude less useful information [51]. It is selected as it improves the relative signal to noise counts through applying convenient parametric or nonparametric techniques [52]. To make it simple, the Wiener filter can be considered as a low-pass imaging filter that is able to be tweaked to the input image's local variance and can be mathematically expressed as in Eq. (8) [50]. The terms: $I_w(x,y)$ is the filtered pixel which is corresponding to the noisy input pixel $I_0(x,y)$, ν expresses the noise variance, μ and σ^2 are the image locally computed mean and standard deviation [53].

$$I_w(x,y) = \mu + \frac{\sigma^2 + \nu^2}{\sigma^2}(I_0(x,y) - \mu) \quad (8)$$

In fact, some hyperspectral bands are negligibly informative. One main reason for certain bands to be less informative is the systemic reduced performance of the HSI optical/ non-optical components. For instance, the low performance might be due to the less uniform illumination spectra or the low detector's quantum efficiency, or both combined. For excluding less informative HSI bands, band/ variable selection (VS) computational process is used. VS is not an arbitrary process since it is executed given a condition of 99 % information within datacube is retained. VS works differently than the dimensionality reduction procedures. The reduction procedures provide its output data with less capability of extracting the high informative bands out of the original ones but VS does. In this study, the matrix low-rank representation (MLRR) [54] is used for achieving VS. MLRR technique is based on sorting the variables in terms of the band self-contained information. To put it simply, MLRR is clustering data pixels drawn from the larger multiple subspaces to delineate outliers. Computing the bands' rank, within a datacube, is accomplished using the Frobenius (element-wise) matrix norm, as follows:

$$X = \sqrt{\sum_{i,j}(X_{i,j})^2}. \quad (9)$$

MLRR clustering starts with calculating the summation for each squared matrix, band-image, columns $\|X\|$ and arrange the columns in a descending order. Then, specifying a threshold percentage value P = 0.99 (significance interval), a comparison between each band, $\|X_k\|$, and the average norm $\left\|\overline{X}\right\|$ of all the bands will highlight outlier bands among the rest:

$$\frac{\|X_k\|}{\left\|\overline{X}\right\|} > P \quad (10)$$

In summary, VS identifies the least informative bands which preserve 99 % of the information in the datacube. By then, the data analysis time for HSI is reduced. To give an example, Fig. 5 displays two rows of images that belong to a single datacube for one participating patient. The top row of images has a very low signal to noise ratio and thus provides less than 1% of the datacubes' information. The elimination of the former bands has a negligible effect on the information of interest. In Fig. 5, the excluded bands (485 nm, 487 nm, and 491 nm) are located in the region that, physiologically, the skin has no distinct features relevant to both hemoglobin chromophores. Instead, the highest informative bands are shown in the bottom row of Fig. 5.

For erythema classification, skin annotations for the distinctly developed skin inflammation are required. For this purpose, annotations

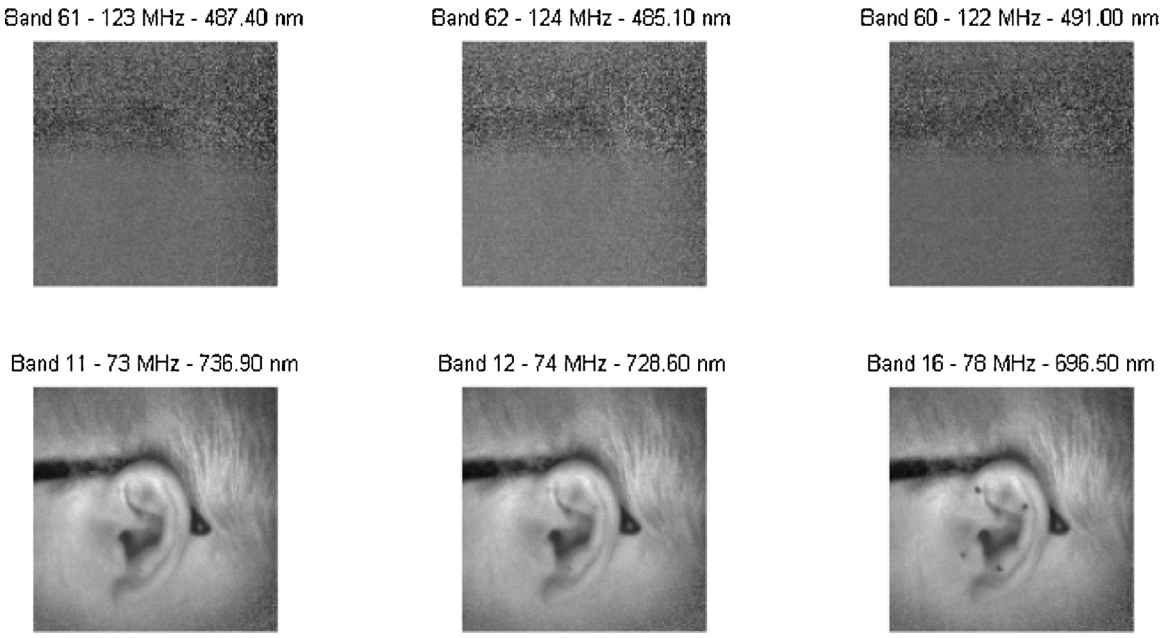

Fig. 5. A display for the least informative bands (485 nm, 487 nm, 491 nm), (top-row), and the highest informative bands (696 nm, 728 nm, 736 nm), (bottom-row) in a single datacube captured for one patient. Both groups of bands were determined by the matrix low-rank representation technique.

were drawn, using Image-J software, by an attending radiotherapist for the study's daily imaging session. The radiotherapist annotations serve are the ground truth data for erythema assessment. The ground truth data is used for the training and cross-validation in the HSI data classification. As the developed erythema is non-homogenously located on the skin region of interest, the radiotherapist annotations do not form mutually exclusive contours. This is a complication for the HSI data classification. To come over this complication, a logic X-OR operation is used to separate the distinct erythema regions and provide exclusive contours for each level as shown in Fig. 6. The non-erythematous skin was used as a reference for healthy skin.

Following the annotation process, the data becomes ready for classification. Among various techniques, we employed the linear discriminant analysis (LDA) [55] method for the HSI data classification. In principle, LDA technique generates a linear transformation matrix H that reduces the spectral k-dimensional raw data of vector F to an s-dimensional vector provided that s < k [56].

$$a = H^T F \; \varepsilon \; \mathbb{R}^s \tag{11}$$

The spectral dimensional reduction is placed on the concept of achieving the maximum possible separation among data classes dissemination [56]. To make it clear, LDA rule of thumb is to maximize the displacement between the central mean point (M) of the distinct classes, meanwhile preserving interclass variance (V) to be minimum [57]. The challenge is to find the axis that projects the data cloud into separate clusters with means $M_1, M_2, \ldots, M_n$ and small variance $V_1, V_2, \ldots, V_n$. For instance, in the case of two classes' mode the term (W), in Eq. (12), represents the plane of best separation, should be maximal to achieve the superlative separation between each class and the other.

$$F(W) = \frac{|M_2 - M_1|}{V_2 - V_1} \tag{12}$$

3. Results and discussion

3.1. Visual assessment

The total score for the erythema VA is determined based on the daily given score by the radiotherapist in response to the daily received

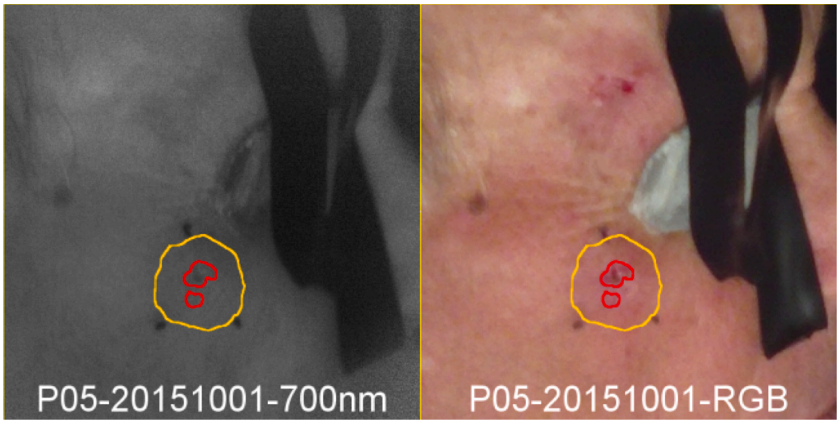

Fig. 6. A sample of annotations created by the radiotherapist to mark two distinct erythema regions as ground truth data. The annotations are overlaid on both spectral data (left) and digital color image (right). The eye shield appeared in the images was put on the patient face for the elimination of light inconvenience during imaging.

fractions of radiation for all patients. Fig. 7 displays the computed VA average score for the participating patients who successfully completed the entire study. The scores were presented against the treatment percentage of completion. The error bars represent the standard deviation of the VA scores among patients. The standard deviation is relatively large since human factors are distinct between patients including age, skin cancer region, and gender. Accumulation of the radiation fractions in the ROI's of the participating patients resulted in a clear increment in the erythema score which is proportional to time.

3.2. Skin reflectance and erythema indices

Once the skin spectral reflectance for the participating patients is computed, it was thought-provoking to monitor the behavior for the skin chromophores indices. Regarding the melanin chromophore, the computed index displayed a fluctuating behavior from one session to the next. Fig. 8 shows the average values for the melanin index for the participating patients while the error bars represent the standard deviation. A dotted black horizontal line is drawn intersecting h the initial level of the apparent melanin prior to receiving any radiation fraction. The purpose of drawing this line is to monitor the melanin index value with respect to the original level for the participating patient. The oscillation in melanin index value all along the radiotherapy treatment time proves that there is no consistent relation between the skin melanin chromophore content and the accumulation of radiation fractions.

In addition to the melanin, corrected and relative erythema indices were calculated for the participating patients by applying Dawson's formulas [47]. The computed melanin-corrected erythema index is exhibited in Fig. 9 while the corresponding relative index is displayed in Fig. 10. A healthy individual subject volunteered to participate in the study. The volunteer is asked to attend an imaging session at the same time on a daily basis for 10 consecutive days maintaining the same routine of imaging, just as participating patients would. The volunteer data was captured according to the study protocol. The corrected and the relative erythema indices were computed and presented in Figs. 9 and 10 for contrast purpose. The error bars for the volunteer case are expressing the standard deviation of the measurement repetitions.

The corrected erythema index showed no trend during the early treatment days, but it increases persistently, at a variable rate, in the second half of the treatment period. We expect that the oscillating behavior for the corrected erythema index is due to fluctuation in the rate of the basal cells destruction in the epidermal layer of the skin [20].

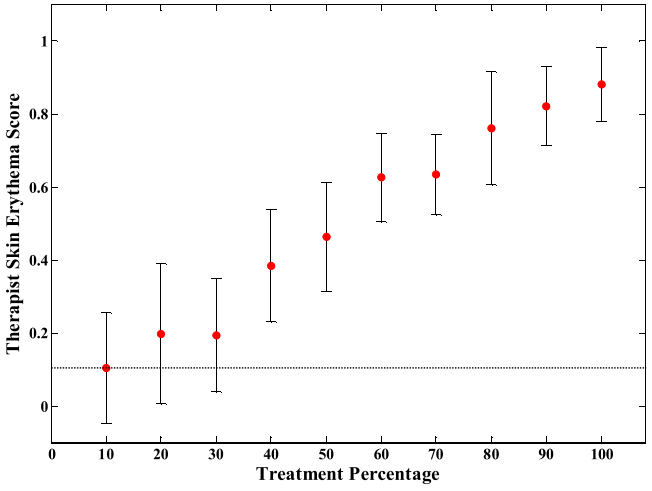

Fig. 7. Visual assessment average score for the recruited patients, who successfully completed the study, during the plan of treatment. The scores are presented against the treatment completion percentage. Error bars represent the standard deviation among patients. A horizontal dotted line is drawn for referencing purpose.

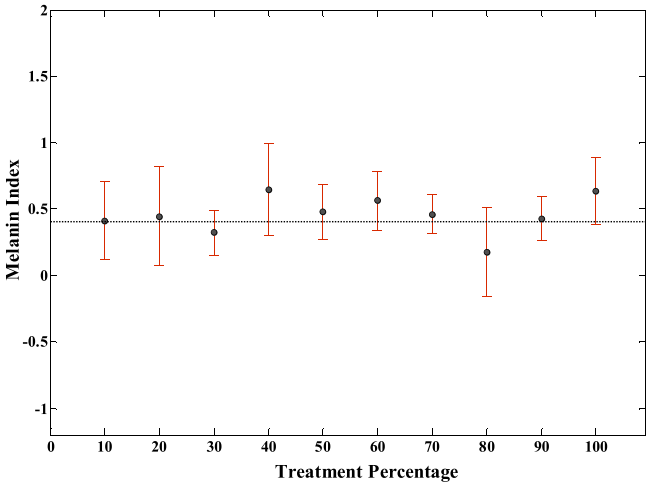

Fig. 8. The study successful Patients' average melanin apparent presence behavior for the entire radiotherapy treatment time are scattered on the data points while the error bars are expressing the variability recorded among patients.

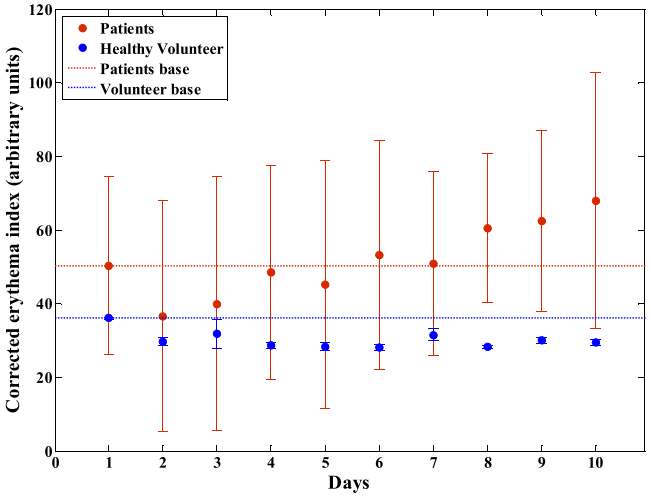

Fig. 9. Displays, in red points, the computed average for melanin corrected erythema index. The error bars express the variability in computed erythema among patients. The red dotted horizontal line is acting as a baseline for **all the subsequent measurements**. The blue points and dotted horizontal line is displaying the volunteer melanin corrected erythema index and baseline, respectively.

Consequently, the inflammatory response of the skin is not consistent. This inconsistent inflammation might be due to the stops in treatment because of weekends, or statutory holidays within the treatment time period. These stops contributed enlarged the error bars. On the volunteer side, the melanin corrected erythema index showed an intermittent alteration with respect to the initial base and small error bars. The volunteer's erythema altered level reflected the daily changes of the skin health status with no clear trend.

The relative erythema index compares skin inflammation in an irradiated body part to a non-irradiated body part. For patients, the relative erythema index displayed a consistent increase against the days of treatment. To confirm the former result, the relative erythema was computed for a healthy volunteer for two distinct regions in his arm. The healthy volunteer data displayed, in Fig. 10, similar values in all the days of imaging except for the baseline measurement. For verification purposes, the former results out of the computed erythema indices need to be statistically significant.

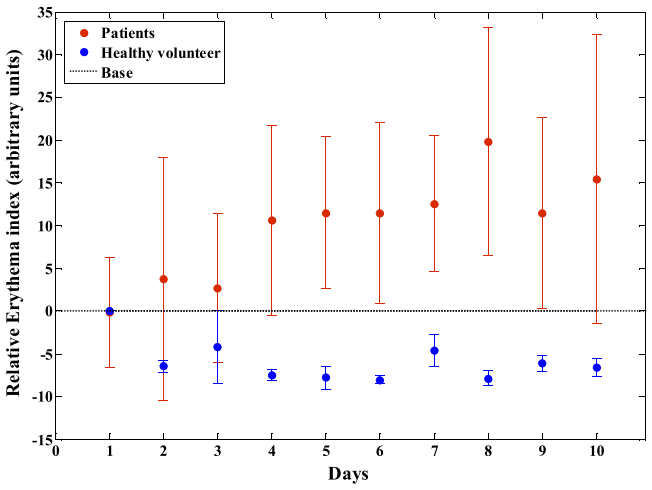

Fig. 10. Displays, in red points, the computed average for relative erythema index. The error bars express the variability in computed relative erythema among patients. The red dotted horizontal line is acting as a baseline for all the subsequent measurement. The blue points and dotted horizontal line display the volunteer relative erythema index and baseline, respectively.

For significance check, Wilcoxon nonparametric two-tail paired test was used to examine the hypothesis of a meaningful difference between the skin's diffuse reflectance at subsequent time points of radiation treatment session against a prior one. Wilcoxon test was utilized in this study, seeing that it works well for a small number of observations. Basically, the Wilcoxon test analyzes the difference in the computed median for two groups of population before and after exposure to a certain experiment [58]. Relative erythema indices, corrected erythema indices, and melanin indices were selected since they are dependent parameters on the skin diffuse reflectance at nine time-points along the radiation treatment plan. Each data point was examined with respect to the initial data point. The examination score is compared to the tabulated Wilcoxon statistical value for the corresponding number of observations. The tabulated Wilcoxon value is plotted as a black horizontal line in Fig. 11(a). This line is the marginal threshold, above which the null hypothesis is rejected. The significance of the Wilcoxon test results is illustrated in Fig. 11(b).

The Wilcoxon test showed that the relative erythema, the corrected erythema, and melanin indices reached and crossed the null rejection threshold at a certain time point through the prescribed radiation treatment period for patients. Markedly, the melanin index has a single time point in the mid-way of the treatment period which crossed the null rejection threshold. As a result, the Wilcoxon statistical test confirmed the inconsistent change in the apparent melanin concentration within the skin due to receiving radiation therapy.

The relative erythema index was the early parameter in terms of time to cross the null hypothesis rejection limit with 90 % significance at the third time point. Furthermore, it reached a significant ratio of 99 % at the seventh time point earlier than the corrected erythema index. This result highlighted the potential of the relative erythema index in delineating the skin response to cancer radiation treatment in a consistent way. It also is evidence of the insignificance of melanin chromophore concentration variability during radiation therapy treatment. So as to approve the benefit of computing erythema indices, it needs to be correlated with visual assessment. For that purpose, the Pearson correlation was computed. The correlation between the visual assessment scores and the corrected erythema index was found to be 79.1 %, and for the relative erythema index was 97.1 %. The former correlation results emphasized the potency of relative erythema index in objectively quantifying skin's reaction toward exposure to radiation.

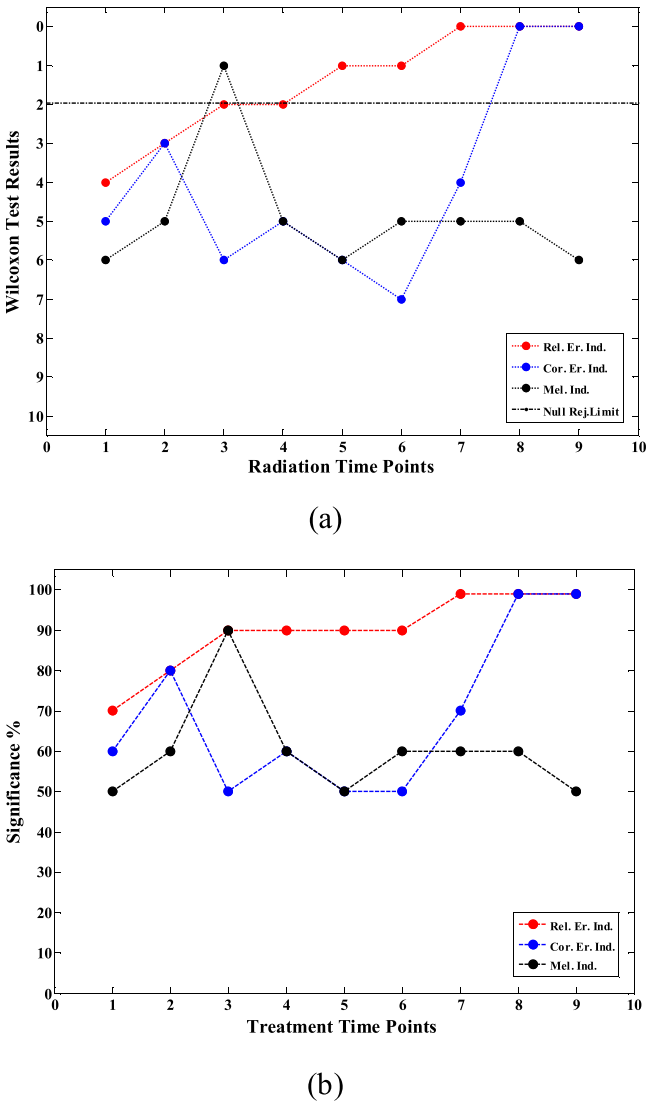

Fig. 11. Wilcoxon (a) statistical test results against null hypothesis rejection limit (no change), (b) corresponding significance percentage for relative erythema, corrected erythema, and melanin indices, along the radiotherapy treatment.

3.3. Estimation of skin chromophores

The main chromophore responsible for the skin's redness/ erythema is the hemoglobin in both oxygenated and non-oxygenated form. Probing apparent hemoglobin concentration is an analytical step in developing a deep understanding of the physiological phenomena accounting for the induced skin inflammation due to radiation exposure. For that purpose, the least-square fitting for the computed reflectance data was accomplished using the extinction function for both hemoglobin forms. This way is used in this study in order to quantitatively estimate hemoglobin apparent concentration during treatment.

The apparent concentration of hemoglobin for involved patients, in this study, were averaged and scattered along the days of treatment as illustrated in Fig. 12(a, b). Error bars represent the variability between the patients. Oxyhemoglobin apparent concentration shows a clear trend of upturn throughout the days of irradiation dose exposure. Deoxyhemoglobin, on the other hand, followed a fluctuating trend. Both hemoglobin components was added to obtain the total apparent hemoglobin concentration displayed in Fig. 12(c). The estimated concentration of the total hemoglobin showed a sporadic trend of ups and downs in the treated body part versus the original concentration before

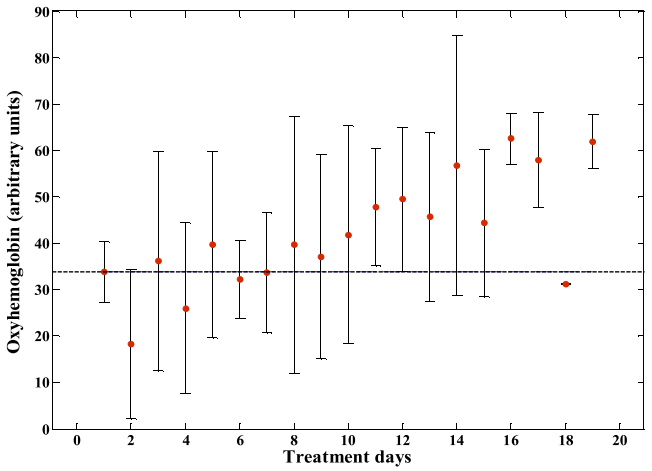

(a)

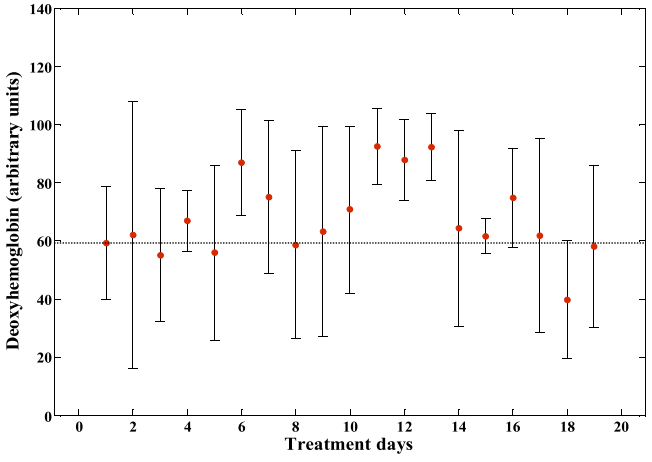

(b)

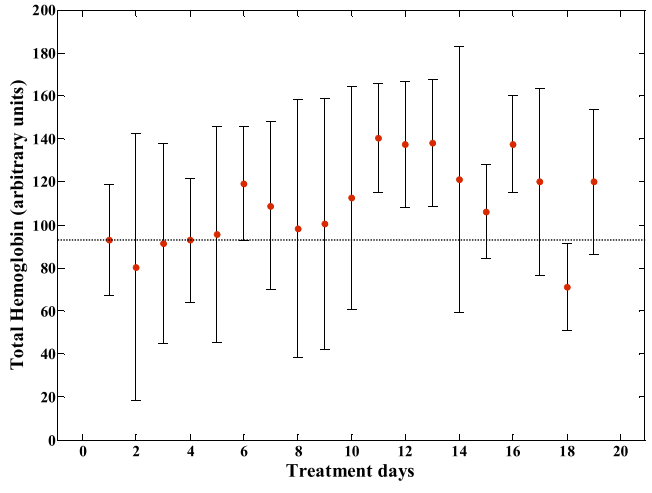

(c)

Fig. 12. Mean Hb-oxy (a), Hb-deoxy (b), and total hemoglobin (c), as a function of time during irradiation. Error bars are displayed representing standard deviation. Baseline values are drawn in each plot in dashed lines, respectively.

irradiation with a general incremental trend. This result is expected due to the unlike temporal apparent concentration behavior acted by both hemoglobin components. Other Potential reasons for the former behavior of the hemoglobin, are (1) the participating patients live different lifestyles throughout the days of treatment, (2) the radiotherapy-induced erythema shows nonhomogeneous spread in the studied region of interest, and (3) the back scattered light might be affected by the variable depth of bone tissues with respect to the treated area of the body.

The inhomogeneity of the induced skin erythema is the result of multiple factors. First, the radiation fields are not homogeneous in dose distribution. Second the region of interest may not receive the same dose due to its physical shape like curved structures such as neck and cheeks or gaps in the face including ears and nose. Third, the erythema response is not simply dependent on the radiation dose alone but both local blood supply and skin pigmentation. As a result, spectral imaging is more appealing than single spot spectroscopy for quantitative assessment of the skin erythema.

3.4. *Image classification*

Applying the developed LDA classifier on both the digital color photographs and the spectral datacubes was the way to contrast both techniques. The contrast was held through a supervised classification for color and spectral data relevant to the ground truth annotations provided by the radiotherapist. Distinct ratios between the training sets and the test sets were examined. Based on the examination, it is found that the 1:1 ratio between training and test samples was superior to other options such as the Pareto principle for 20:80 percentage, as well as other 60:40 % percentage. The 1:1 ratio produced satisfactory results for most of the assessment parameters. The hyperspectral system shows comparable performance to digital photography in parameters such as accuracy and sensitivity while it outperforms RGB imaging in specificity and the geometrical mean. We report the classification results for six statistical parameters. The classification procedure was repeated for ten times, in each time training and test sets were randomly selected out of the population data in order to verify the reliability of the classification results. The results of the data classification are displayed in Table 3.

4. Conclusion

This pilot study provides an evidence that support the use of optics-based technology as an objective approach for clinical assessment of skin erythema. In particular, HSI permitted contactless visualization and quantitative assessment of relatively wide skin region in terms of oxygenation and perfusion in radiotherapy, which is time efficient in contrast to diffuse reflectance spectroscopy. We conclude the results of this study as follows:

1 The relative erythema index value at the 7th radiation session varies with 99 % significance compared against non-irradiated skin. Relative erythema index is verified to be the most sensitive parameter to assess the skin response due to irradiation, as it achieved a 97.1 % correlation ratio relative to visual assessment of erythema.
2 Oxyhemoglobin chromophore concentration showed a gradual increase along with radiation accumulation in the areas adjacent to the lesion. This increase in hemoglobin concentration is probably due to the skin healing process after damage. Conversely, deoxyhemoglobin showed an oscillating behavior through the radiation period.
3 The supervised erythema classification based on HSI data tremendously outperformed RGB imaging in terms of specificity and geometric mean.

The future development of improved sources of illumination and the reduction of the instrumentation noise level will help pave the way for HSI to become a fast, reliable, and, above all, objective quantitative

Table 3
Classification results for comparison between HSI and RGB imaging regarding skin erythema assessment.

Technique	Accuracy	Precision	F-measure	Sensitivity	Specificity	G-mean
HSI-Imaging	91.08 ± 0.83	85.23 ± 0.98	86.65 ± 0.89	88.68 ± 1.01	32.89 ± 3.39	47.23 ± 2.63
RGB- Imaging	91.28 ± 0.50	83.23 ± 1.99	86.2 ± 0. 94	90.10 ± 0.94	16.85 ± 4.63	25.08 ± 6.59

method for erythema classification. Further experimental, clinical, and analytical work needs to be done to validate HSI as a real-time clinical instrument.

Acknowledgements

RA was supported by funding from the Military Technical College of Egypt. This project was supported in part by the Natural Science and Engineering Research Council (NSERC) of Canada (#1067403, QF), Canadian Foundation of Innovation (CFI, QF), the Province of Ontario (ORF-RI, QF), and the Juravinski Hospital and Cancer Foundation (LDW, TJF, JEH). QF held the Canada Research Chair in Biophotonics. The authors thank Prof. Josiane Zerubia from INRIA Sophia-Antipolis Méditerranée for valuable discussions in imaging classification algorithms.

References

[1] A.C. Society, Cancer Facts & Figures 2015, 2015.
[2] M. Veness, S. Richards, Role of modern radiotherapy in treating skin cancer, Australas. J. Dermatol. 44 (3) (2003) 159–166, quiz 167–168.
[3] N.P. Nguyen, et al., Effectiveness of radiotherapy for elderly patients with non-melanoma skin cancer of the head, Geriatr. Gerontol. Int. 15 (5) (2015) 601–605.
[4] A. Sanabria, A.L. Carvalho, J.G. Vartanian, J. Magrin, M.K. Ikeda, L.P. Kowalski, Comorbidity is a prognostic factor in elderly patients with head and neck cancer, Ann. Surg. Oncol. 14 (4) (2007) 1449–1457.
[5] D.M. Brizel, R.K. Dodge, R.W. Clough, M.W. Dewhirst, Oxygenation of head and neck cancer: changes during radiotherapy and impact on treatment outcome, Radiother. Oncol. 53 (1999) 113–117.
[6] M. Caccialanza, R. Piccinno, L. Kolesnikova, L. Gnecchi, Radiotherapy of skin carcinomas of the pinna: a study of 115 lesions in 108 patients, Int. J. Dermatol. 44 (6) (2005) 513–517.
[7] W. Maddocks-Jennings, J.M. Wilkinson, D. Shillington, Novel approaches to radiotherapy-induced skin reactions: a literature review, Complement. Ther. Clin. Pract. 11 (4) (2005) 224–231.
[8] D. Porock, L. Kristjanson, Skin reactions during radiotherapy for breast cancer: the use and impact of topical agents and dressings, Eur. J. Cancer Care (Engl.) 8 (3) (1999) 143–153.
[9] S.K. MacBride, M.E. Wells, C. Hornsby, L. Sharp, K. Finnila, L. Downie, A case study to evaluate a new soft silicone dressing, Mepilex Lite, for patients with radiation skin reactions, Cancer Nurs. 31 (1) (2008) E8–E14.
[10] S. D'haese, M. Van Roy, T. Bate, P. Bijdekerke, V. Vinh-Hung, Management of skin reactions during radiotherapy in Flanders (Belgium): a study of nursing practice before and after the introduction of a skin care protocol, Eur. J. Oncol. Nurs. 14 (5) (2010) 367–372.
[11] J.W. Denham, et al., Factors influencing the degree of erythematous skin reactions in humans, Radiother. Oncol. 36 (2) (1995) 107–120.
[12] M. McQuestion, Evidence-based skin care management in radiation therapy, Semin. Oncol. Nurs. 22 (3) (2006) 163–173.
[13] N. Lee, et al., Skin toxicity due to intensity-modulated radiotherapy for head-and-neck carcinoma, Int. J. Radiat. Oncol. Biol. Phys. 53 (3) (2002) 630–637.
[14] N. Salvo, et al., Prophylaxis and management of acute radiation-induced skin reactions: a systematic review of the literature, Curr. Oncol. 17 (4) (2010) 94–112.
[15] E.J. Yoshida, H. Chen, M.A. Torres, W.J. Curran, T. Liu, Spectrophotometer and ultrasound evaluation of late toxicity following breast-cancer radiotherapy, Med. Phys. 38 (10) (2011) 5747–5755.
[16] D. Yohan, et al., Quantitative monitoring of radiation induced skin toxicities in nude mice using optical biomarkers measured from diffuse optical reflectance spectroscopy, Biomed. Opt. Express 5 (5) (2014) 1309–1320.
[17] F. De Felice, A. Galdieri, G. Abate, N. Bulzonetti, D. Musio, V. Tombolini, Definitive intensity-modulated radiation therapy in elderly patients with locally advanced oropharyngeal cancer, In Vivo (Brooklyn) 31 (3) (2017) 455–459.
[18] A.I. Ilich, et al., Effects of gender on capecitabine toxicity in colorectal cancer, J. Oncol. Pharm. Pract. 22 (3) (2016) 454–460.
[19] Y. van Wijk, et al., Development of a virtual spacer to support the decision for the placement of an implantable rectum spacer for prostate cancer radiotherapy: comparison of dose, toxicity and cost-effectiveness, Radiother. Oncol. 125 (1) (2017) 107–112.
[20] R.I.J.W. Hopewell, (CRC Normal Tissue Radiobiology Research Group and H. (University of Oxford), The Churchill Hospital, The skin : its structure and response to ionizing radiation, Int. J. Radiat. Biol. 57 (4) (1990) 751–773.
[22] R. Abdlaty, et al., Hyperspectral imaging and classification for grading skin erythema, Front. Phys. 6 (August) (2018) 1–10.
[23] S. Wan, J. a Parrish, K.F. Jaenicke, Quantitative evaluation of ultraviolet induced erythema, Photochem. Photobiol. 37 (6) (1983) 643–648.
[24] B.L. Diffey, R.J. Oliver, P.M. Farr, A portable instrument for quantifying erythema induced by ultraviolet radiation, Br. J. Dermatol. 111 (December (6)) (1984) 663–672.
[25] C. Balas, An imaging colorimeter for noncontact tissue color mapping, IEEE Trans. Biomed. Eng. 44 (6) (1997) 468–474.
[26] J. Nyström, P. Geladi, B. Lindholm-Sethson, J. Rattfelt, A.C. Svensk, L. Franzen, Objective measurements of radiotherapy-induced erythema, Skin Res. Technol. 10 (4) (2004) 242–250.
[27] C.K. Kraemer, D.B. Menegon, T.F. Cestari, Determination of the minimal phototoxic dose and colorimetry in psoralen plus ultraviolet A radiation therapy, Photodermatol. Photoimmunol. Photomed. 21 (5) (2005) 242–248.
[28] G.N. Stamatas, B.Z. Zmudzka, N. Kollias, J.Z. Beer, In vivo measurement of skin erythema and pigmentation: new means of implementation of diffuse reflectance spectroscopy with a commercial instrument, Br. J. Dermatol. 159 (3) (2008) 683–690.
[29] S. Taylor, W. Westerhof, S. Im, J. Lim, Noninvasive techniques for the evaluation of skin color, J. Am. Acad. Dermatol. 54 (5) (2006) S282–S290.
[30] K. Vishwanath, D. Klein, K. Chang, T. Schroeder, M.W. Dewhirst, N. Ramanujam, Quantitative optical spectroscopy can identify long-term local tumor control in irradiated murine head and neck xenografts, J. Biomed. Opt. 14 (5) (2009) 054051.
[31] D.L. Glennie, J.E. Hayward, D.E. Mckee, T.J. Farrell, Inexpensive diffuse reflectance spectroscopy system for measuring changes in tissue optical properties, J. Biomed. Opt. 19 (December) (2014), pp. 105005-1-105005–105006.
[32] D. Yohan, et al., Quantitative monitoring of radiation induced skin toxicities in nude mice using optical biomarkers measured from diffuse optical reflectance spectroscopy, Biomed. Opt. Express 5 (5) (2014) 1309–1320.
[33] M. Setaro, A. Sparavigna, Quantification of erythema using digital camera and computer-based colour image analysis: a multicentre study, Skin Res. Technol. 8 (2002) 84–88.
[34] S.G. Coelho, S.A. Miller, B.Z. Zmudzka, J.Z. Beer, Quantification of UV-induced erythema and pigmentation using computer-assisted digital image evaluation, Photochem. Photobiol. 82 (3) (2006) 651–655.
[35] E. Rizova, A. Kligman, New photographic techniques for clinical evaluation of acne, J. Eur. Acad. Dermatol. Venereol. 15 (Suppl. 3) (2001) 13–18.
[36] H. Huang, L. Liu, M.O. Ngadi, Recent developments in hyperspectral imaging for assessment of food quality and safety, Sensors (Basel) 14 (January (4)) (2014) 7248–7276.
[37] P. Mishra, M.S.M. Asaari, A. Herrero-Langreo, S. Lohumi, B. Diezma, P. Scheunders, Close range hyperspectral imaging of plants: a review, Biosyst. Eng. 164 (December) (2017) 49–67.
[38] D. Nishijima, M.I. Patino, R.P. Doerner, New application of hyperspectral imaging to steady-state plasma observations new application of hyperspectral imaging to steady-state plasma observations, Rev. Sci. Instrum. 083501 (August) (2020).
[39] R. Abdlaty, M. Gobara, I. Naiem, M. Mokhtar, Innovative technique for analysis of wastewater contaminants using hyperspectral imaging, J. Spectral. Imaging 9 (2020) 1–10.
[40] M.A. Calin, S.V. Parasca, D.A.N. Savastru, D. Manea, Hyperspectral imaging in the medical field: present and Future, Appl. Spectrosc. Rev. 49 (2014) 435–447.
[41] R. Abdlaty, J. Orepoulos, P. Sinclair, R. Berman, Q. Fang, High throughput AOTF hyperspectral imager for randomly polarized light, Photonics 5 (1) (2018) 3.
[42] R. Abdlaty, Q. Fang, Acousto-optic tunable filter-based hyperspectral imaging system characterization, Proc. SPIE 10870, Design and Quality for Biomedical Technologies XII (2019) no. February.
[43] C. a Schneider, W.S. Rasband, K.W. Eliceiri, NIH Image to ImageJ: 25 years of image analysis, Nat. Methods 9 (7) (2012) 671–675.
[44] G.N. Stamatas, N. Kollias, In vivo documentation of cutaneous inflammation using spectral imaging, J. Biomed. Opt. 12 (5) (2007) 051603.
[45] T. Lister, P. a Wright, P.H. Chappell, Optical properties of human skin, J. Biomed. Opt. 17 (September (9)) (2012), pp. 90901–1.
[46] F.H. Mustafa, M.S. Jaafar, Comparison of wavelength-dependent penetration depths of lasers in different types of skin in photodynamic therapy, Indian J. Phys. 87 (November (3)) (2012) 203–209.
[47] J.B. Dawson, et al., A theoretical and experimental study of light absorption and scattering by in vivo skin, Phys. Med. Biol. 25 (4) (1980) 695–709.
[48] D.L. Glennie, J.E. Hayward, D.E. Mckee, T.J. Farrell, Inexpensive diffuse reflectance spectroscopy system for measuring changes in tissue optical properties, J. Biomed. Opt. 19 (December) (2014) 1–6.
[49] D.L. Glennie, J.E. Hayward, T.J. Farrell, Modelling Changes in Skin Blood Concentration with Total Diffuse Reflectance Spectroscopy, 2021, pp. 1–31.
[50] S. Tan, R. Young, D. Budgett, J. Richardson, C. Chatwin, A pattern recognition Weiner filter for realistic clutter backgrounds, Opt. Commun. 172 (1–6) (1999) 193–202.

[51] M. Isaac, N. Bankman, Applied physics laboratory Johns Hopkins University Laurel. Handbook of Medical Imaging, Academic Press, 2000.
[52] T. Wang, Ö. Özdamar, J. Bohórquez, Q. Shen, M. Cheour, Wiener filter deconvolution of overlapping evoked potentials, J. Neurosci. Methods 158 (2) (2006) 260–270.
[53] Fundametals of Digital Image Processing, Prentice Hall, 1989.
[54] G. Liu, Z. Lin, S. Yan, J. Sun, Y. Yu, Y. Ma, Robust recovery of subspace structures by low-rank representation, Pattern Anal. Mach. Intell. IEEE Trans. 35 (1) (2013) 171–184.
[55] M. Li, B. Yuan, 2D-LDA: a statistical linear discriminant analysis for image matrix, Pattern Recognit. Lett. 26 (5) (2005) 527–532.
[56] T. Bandos, Classification of hyperspectral images with regularized linear discriminant analysis, Geosci. Remote 47 (3) (2009) 862–873.
[57] U. of T. Welling, Max (Department of Computer Science, "Fisher Linear Discriminant Analysis," 2005.
[58] M.H. Shilts, et al., Minimally invasive sampling method identifies differences in taxonomic richness of nasal microbiomes in young infants associated with mode of delivery - online first - springer, Microb. Ecol. (2016) 233–242.
[59] R. Abdlaty, Q. Fang, T.J. Farrell, J.E. Hayward, Skin erythema and pigmentation: a review of optical assessment techniques, Photodiagn. Photodyn. Ther. 33 (2020).